Energy Technology
Generation, Conversion, Storage, Distribution
www.entechnol.de

Image-Based Quantification of Deposited Lithium on Li Metal Surfaces

Hannes Kühnle, Sascha Berg, Susanne Frese, Edwin Knobbe, and Egbert Figgemeier**

Image-based quantification of the amount of deposited lithium on Li metal surfaces remains a big challenge. This work introduces an automated workflow consisting of the following steps: pixel-wise identification of deposited lithium, segmentation of pixel clusters in instances of deposited Li structures, and instance-based quantification of deposited lithium. Two algorithms for the identification of deposited lithium are developed. The rule-based approach uses a combination of logical filters to detect deposited lithium. Core element of the neural network-based approach is a single convolution neural network. Images of deposited lithium on Li electrodes in a Li||Li in situ cell are used as input data. Selected images are manually masked to generate data to optimize, train, and evaluate the performance of both image processing approaches. Segmentation enables to quantify instances of deposited Li structures by number, characteristic length scale, and volume. Automated image processing makes the assessment of the total deposited volume of lithium at the end of a constant current phase feasible, as well as the evolution of the total deposited volume during the constant current phase for various current densities.

1. Introduction

Lithium metal electrodes are one potential path to develop battery cells with higher energy densities in comparison to lithium-ion batteries.[1–3] However, low Coulomb efficiency[4] as well as the formation of voluminous and potentially harmful deposited Li structures still hinder commercialization.[5–7] One approach to study the deposition behavior of lithium is to use an optically accessible battery cell with a transparent liquid electrolyte, which the authors developed in previous work.[8] A challenge with image-based methods is to quantify the amount of deposited lithium. For example, in Ref. [9], the authors observed the dendrite formation in the cross-section through a transparent side wall in a Li|LPSC|LPSC-PTFE|LPSC|Cu solid-state electrolyte cell but only evaluated the data in a qualitative analysis. Romio et al.[10] used an operando optical microscope in a modified coin cell setup featuring a transparent indium tin oxide-polyethylene terephthalate window as the current collector. They used an automated image evaluation to count the number of separable depositions (referred to as "blobs") and their mean radius to calculate the "blob area". Since they only used 2D from the top, the deposition volume could not be quantified.

The authors of this work investigated in a previous study[8,11] the influence of current density on the deposition behavior of lithium on a Li metal surface. Separate deposition regimes with distinctive morphological and electrochemical properties were discovered at lower and higher current densities, respectively, including a transition region between those regimes. An instance was defined as a deposited Li structure that grows from a single seed point on the electrode. The amount of deposited lithium was quantified by three parameters: number of instances, characteristic length scale of instances, and total deposited lithium volume. Image processing was performed manually, and only the final image at the end of the constant current phase was used. Instances smaller than 0.2 mm were ignored in the evaluation since they could not be manually identified. At higher current densities, the number of instances increased exponentially and could not be individually evaluated, so they had to be approximated by representative mean values. Assessments from the previous paper[8] will be referred to as manual evaluation approach (MEA) in this work.

H. Kühnle, S. Frese, E. Figgemeier
Institute for Power Electronics and Electrical Drives (ISEA)
RWTH Aachen University
52074 Aachen, Germany
E-mail: e.figgemeier@fz-juelich.de

S. Berg, E. Figgemeier
IMD-4
Helmholtz Institute Münster (HI MS)
Forschungszentrum Jülich
52074 Aachen, Germany
E-mail: s.berg@fz-juelich.de

E. Knobbe
BMW Group
Battery Cell Competence Centre
80788 Munich, Germany

E. Figgemeier
JARA-Energy
Juelich Aachen Research Alliance
52425 Jülich, Germany

The ORCID identification number(s) for the author(s) of this article can be found under https://doi.org/10.1002/ente.202500364.

DOI: 10.1002/ente.202500364

Automated image processing tools are required to resolve the issues of the MEA at lower and higher current densities, increase objectivity and processing speed, and enable assessments that are not feasible to be performed by hand. There are three main steps in an image-based method to quantify the amount of deposited lithium on Li metal surfaces: 1) pixel-wise identification of deposited lithium to generate pixel clusters with deposited lithium; 2) segmentation of pixel clusters into individual instances with deposited lithium; and 3) instance-based quantification of deposited lithium (e.g., number, length scale, or total volume).

This work introduces two automated methods for the pixel-wise identification of deposited lithium: the rule-based approach (RBA) and the neural network-based approach (NNBA). Both approaches together with the segmentation and quantification algorithms have been implemented in MATLAB (R2021b, The MathWorks Inc.).

The first challenge was to distinguish pixels that show deposited lithium from pixels that show Li metal of the electrode surface, where both cases have a metallic silver color (identification algorithm). Reflections from the cell casing on the electrode surface caused an inhomogeneous grayish background at the electrode surface in the image. Deposited Li structures growing on the electrode surface interacted with the incident light. Due to their fractal surface, they showed a wide range of gray tones due to different textures, light intensities, reflections, absorptions, or shadows. For the second challenge, agglomerations of pixels identified as deposited lithium had to be segmented into individual instances of deposited Li structures with the corresponding seed points (segmentation algorithm). Solving this second challenge made it possible to quantify the number of instances and determine the characteristic length scale of every instance. Based on the characteristic length scale, the volume of every instance could be approximated and the total deposited lithium volume could be calculated.

2. Automatic Detection of Deposited Lithium

2.1. Experimental Section

In a previously published work,[8] image recordings of deposited lithium have been obtained in an optically accessible cell with two Li metal electrodes and a transparent liquid electrolyte. Li foils (electrodes) from the same production batch were distributed over two pouch bags, which were consecutively used for these experiments. Electrochemical data indicated that the Li foils from both bags experienced different aging, which was observed after all experiments were concluded, although they were stored under inert gas conditions (Ar-atmosphere, $H_2O < 1$ ppm, $O_2 < 1$ ppm). This work only used the images of the previous work to develop automated image processing algorithms to quantify deposited lithium on a Li metal surface.

Every experiment had a well-defined starting point to equilibrate the electrochemical system. This was followed by a phase with constant current (CC) at various current densities, where every experiment had the same total amount of charge throughput equal to $Q_{\text{total}} = 10.9$ mAh. The experiments were performed with nine current densities: $J = 0.05$, 0.1, 0.25, 0.5, 0.75, 1, 2, 5, and 10 mA cm^{-2}. The experiment was repeated five times for every current density, so there was a total of 45 experiments. The active electrode surface was equal to $A_{\text{active}} = 13.08$ cm^2, which was used to set the CC corresponding to the required current density. Consequently, the duration $t_{\text{CC-phase}}$ of the CC phase was not identical for every current density (see **Table 1**).

Images were recorded with a 5x magnification and a 30° recording angle (KEYENCE VHX-6000 digital microscope with KEYENCE VH-Z00T zoom lens 0x–50x). The recorded images were saved in an 8-bit RGB, lossless, and compression-free image file format (*.tif). In most cases, images were recorded every 60 s during the CC phase, which resulted in a larger charge throughput Q_{sample} between two recorded images for increasing current densities. Furthermore, this would decrease the number of recorded images from $N_{\text{sample}} = 1000$ at $J = 0.05$ mA cm^{-2} to $N_{\text{sample}} = 20$ at $J = 10$ mA cm^{-2}. The time interval between the two recorded images was therefore reduced to 15 s for the highest current densities. At lower current densities, the number of images was limited to $N_{\text{eval}} = 100$ to reduce the calculation time during the development of the automated algorithms. The image recording and processing settings are summarized in Table 1. Notice that the first image of the CC phase was recorded after the charge was transferred, so the number of images was equal to the number of intervals.

Table 1. Settings for image recording and processing as a function of current density in Kühnle et al.[8] Symbols denote: $t_{\text{CC-phase}}$ duration of CC-phase, t_{sample} time between two images, N_{sample} number of recorded images, Q_{sample} charge throughput between two recorded images, N_{eval} number of processed images, and Q_{eval} charge throughput between two processed images.

	Measurement		Image recording			Image processing	
	J mA cm^{-2}	$t_{\text{CC-phase}}$ s	t_{sample} s	N_{sample}	Q_{sample} µAh	N_{eval}	Q_{eval} µAh
Low J (Regime 1)	0.05	60 000	60	1000	5.45	100	54.5
	0.1	30 000	60	500	10.9	100	54.5
	0.25	12 000	60	200	21.8	100	54.5
	0.5	6,000	60	100	54.5	100	54.5
Medium J (Transition)	0.75	4,000	60	67	163.5	67	163.5
	1	3,000	60	50	218	50	218
High J (Regime 2)	2	1,500	60	25	436	25	436
	5	600	15	40	272.5	40	272.5
	10	300	15	20	545	20	545

2.2. Image Preprocessing

Optimization, training, and performance evaluation of the automated image processing approaches required preprocessing to generate the appropriate data. Image pixels corresponding to deposited lithium were manually masked (shown in red in **Figure 1**c) using the open-source raster graphics editor GIMP (2.10.20, The GIMP Development Team). Notice that connected masked pixels could be agglomerations of deposited Li structures. The resulting masks provided a binary classification between pixels with deposited lithium and pixels with all other kinds of information. The manual masking process was repeated by a second person, which resulted in two distinctive masks, and the difference is quantified in **Figure 2**. The distinction in those two masks showed how challenging it is to obtain objective information from image data.

The line-of-sight of the microscope had an angle of 30° with respect to the surface of the electrode, which generates a perspective distortion in the images of electrodes and deposited lithium. Four corner points (Figure 1c, yellow triangles) defined an observed area of the electrode (Figure 1d, yellow rectangle) that will be considered for all analyses in this work. This observed electrode area measured 4.35 × 2.75 cm and had a surface area of $A_{\text{observed}} = 11.96\ \text{cm}^2$. First, a distortion correction was applied to the images using the intrinsic camera parameters which were determined with recorded images of a checkerboard pattern. Next, the images were converted to gray scale images because the color channels were not offering additional information due to the low color spectrum in the images (similar shades of gray). In the third step, the corner points of the observed electrode area were manually set for each experiment because automated corner point detection algorithms did not work precise enough. This was the only manual step in the automated scripts. Finally, a keystone correction using projective transformation[12] was performed on the distorted image. None of these image preprocessing steps were performed during the MEA in the previous work.[8]

2.3. The RBA to Identify Pixel Clusters with Lithium Deposition

The first approach to identify pixel clusters with deposited lithium is based on a pixel-wise assessment by binary combinations of multiple filters and will therefore be denoted as the RBA. Separate sets of filter combinations were developed for low, medium, and high current densities, respectively, in the domains: regime 1, transition region, and regime 2 (see Table 1). The current densities of $J = 0.1\ \text{mA cm}^{-2}$, $J = 1\ \text{mA cm}^{-2}$, and $J = 10\ \text{mA cm}^{-2}$ were selected to be representative of the development of the filter sets of the corresponding domains. For every experiment, the automated image processing was applied to the complete series of up to 100 images, but only the masked image at the end of the CC phase was used to quantify the optimization of the filter parameters.

Operation of the applied filter algorithms, which were combined for the pixel identification in the RBA, is briefly explained in the following: 1) **Blurred summed previous difference (*SumPrevDiff*)**: This filter uses Gaussian blurring with a 3 × 3 kernel to reduce the influence of noise that is caused due to the long duration of an experiment. The summed previous difference takes the difference between the current and previous image from the recorded series and binarizes the result using a threshold generated with Otsu's method.[13,14] All pixels that

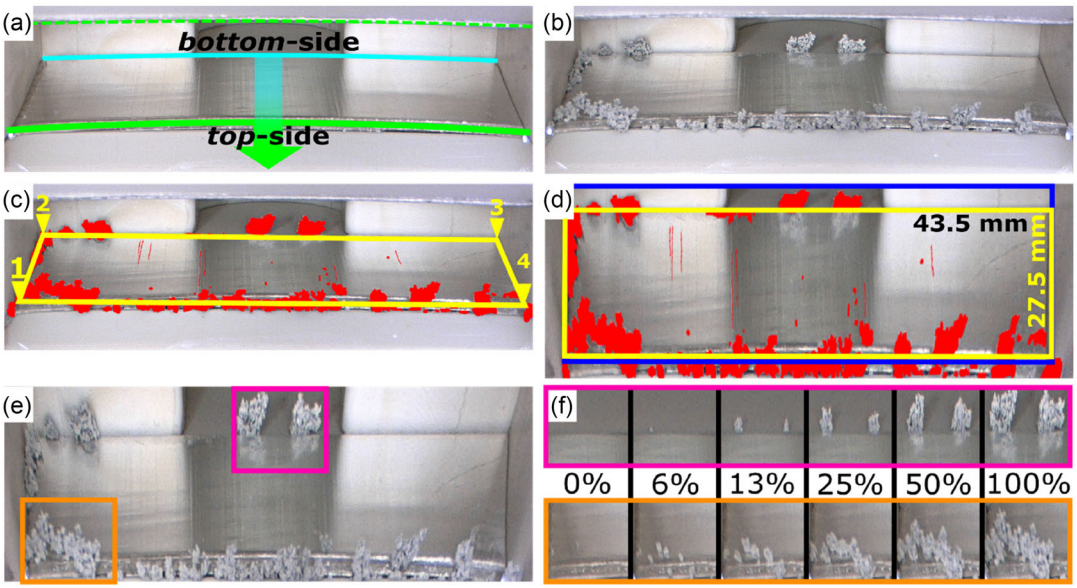

Figure 1. Example image at a current density of $J = 0.75\ \text{mA cm}^{-2}$. a) Pristine electrode surface before the charge is transferred. b) Electrode with deposited Li structures after the charge is transferred. c) Manually generated, pixel-based mask of deposited Li structures (shown in red). The four yellow triangles define the corner points of the electrode plateau. d) Image with manually generated mask (red) after image preprocessing. Yellow rectangle: area considered for performance evaluation of image identification approaches. Blue rectangle: area where deposited Li structures are evaluated (see Figure 6). e) Image after image preprocessing with two rectangles (magenta and orange) to mark the areas shown in (f). f) Lithium growth at distinct steps for two exemplary areas during the deposition process. The numbers give the percentage of charge transferred.

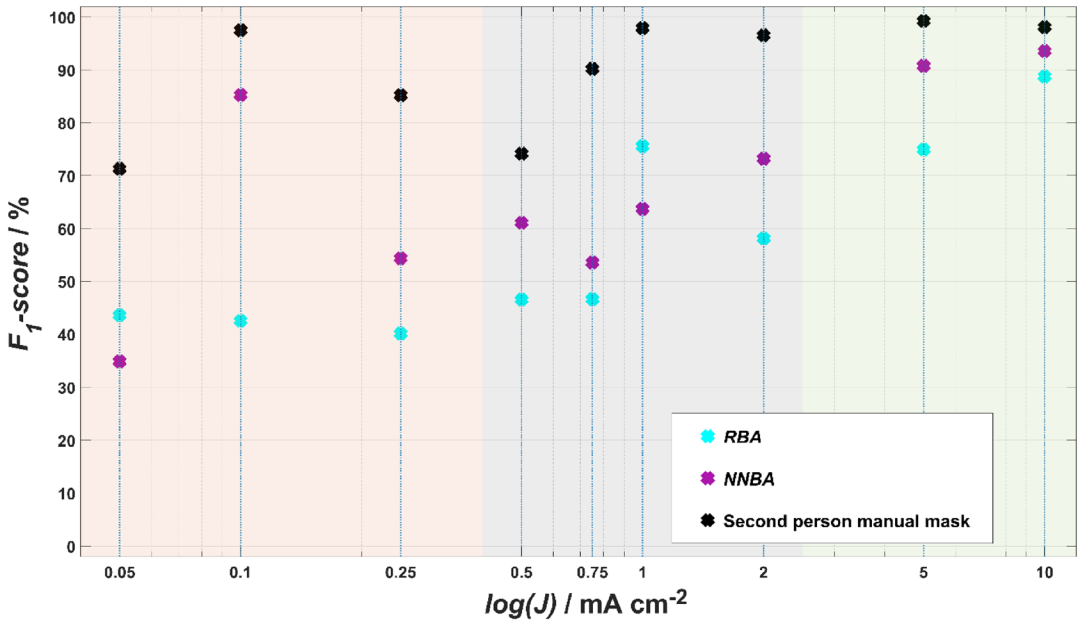

Figure 2. F_1-scores of the identification process for the evaluation experiments with RBA, NNBA, and masking by a second person. Reference for this analysis is a manually obtained mask by a first person.

have been set to true in this filter will remain true for the following images in this series; 2) **Blurred morphological opening (*BlurOpen*):** Performing a morphological opening on a grayscale image will set all pixels inside a structuring element to the lowest grayscale value of the element.[15] Subtracting the individual pixel values of the original image from its image background computed by a morphological opening results in a grayscale image where only those removed instances are shown; 3) **Red cast filter** (***RedCast***): At lower current densities, fine structures sometimes showed some red cast on their edges. This red cast is detected and smoothed by morphological closing using a disk with a diameter of 3 pixels as a structuring element; 4) **Absolute difference (*AbsDiff*):** In the *RBA*, it is assumed that the first image of the series shows a surface with no deposited lithium. These pixel values are stored as an initial state of the electrode. Next, all further images in the series are processed sequentially. Deviations in the pixels between 1) the current image and the initial image as well as between 2) the current image and the corresponding previous image in the series are detected and will be counted as potential deposited lithium. There were two separate thresholds that were initially optimized using the manually generated masks; 5) **Mean value difference** (***MeanDiff***): The mean value of a single pixel over all previous images is calculated for every image in the series, which results in a series of corresponding mean value images. The binary image is obtained from the difference of the current image with the respective mean value image; 6) **Morphological opening (*MorphOpen*):** The morphological opening for medium and high current densities were performed without the application of a Gaussian blur. The structuring elements are disks with a diameter of 15 pixels for medium and 10 pixels for high current densities; 7) **Image edge detection (*EdgeDetect*):** Several methods to detect edges of objects in images are available. The Sobel algorithm[16–18] was used because of its feature to filter objects specifically according to their edge direction. The detected edges are then smoothed by morphological closing using a disk with a diameter of three pixels as a structuring element; 8) **Preserving difference noise filter** (***SummedDiff***): The difference between the current image and the previous image in the series is calculated and binarized using a threshold. Once a pixel has been identified as true, it will remain true for all following images in the series.

All voids in closed pixel conglomerates were filled after the binary images were obtained from the algorithms (except *SummedDiff*). Application of a filter to an image resulted in a matrix tf_{filter} with binary values (true-false), hence

$$tf_{\text{filter}} = \text{Filter}(\text{image}) \tag{1}$$

To describe binary filter combinations, the pixel-wise binary operator 'and' will be denoted as & and the pixel-wise binary operator 'or' is denoted as |. The combination of the filter algorithms was chosen individually for low, medium, and high current densities and accounted for typical (visual) key deposition characteristics of the corresponding domain.

At low current densities, the electrode surface showed predominantly flat, partially parallel-oriented, lamellar patterns of deposited Li structures. These structures are very thin compared to much larger and voluminous structures at high current densities. The developed filter combination for low current densities can be formulated as

$$tf_{\text{low}} = (tf_{\text{SumPrevDiff}} \,|\, tf_{\text{BlurOpen}} \,|\, tf_{\text{RedCast}}) \tag{2}$$

At medium current densities, the images showed a combination of many, tiny, lamellar deposited Li structures, mixed with a

smaller fraction of large, deposited Li structures. Furthermore, the center region of the electrode had a higher contrast when compared to the edge regions of the electrode. A consequence was different numbers of positively identified pixels per area for these regions. An indicator for growth of tiny lamellar structures was set, when this number for the center region was at least double the number for the edge region. If this indicator is triggered frequently after the fifth image in the series, then the binary image is determined at the edge region of the electrode with significantly higher recall for all following images (lower threshold for binarization). The filter combination to obtain the binary matrix tf_{medium} for medium current densities in the transition region is shown in the formula:

$$\mathrm{tf}_{\mathrm{medium}} = (tf_{\mathrm{AbsDiff}} \ \& \ tf_{\mathrm{MorphOpen}}) \,|\, (tf_{\mathrm{AbsDiff}} \ \& \ tf_{\mathrm{EdgeDetect}}) \,|\, (tf_{\mathrm{MorphOpen}} \ \& \ tf_{\mathrm{EdgeDetect}}) \quad (3)$$

At high current densities, individual instances of deposited Li structures are small, evenly distributed and densely packed on top of the electrode surface. The best performance at high current densities was obtained with the filter combination resulting in the binary matrix tf_{high}

$$tf_{\mathrm{high}} = (tf_{\mathrm{SummedDiff}} \,|\, tf_{\mathrm{MorphOpen}}) \ \& \ tf_{\mathrm{MeanDiff}} \quad (4)$$

The developed filter combinations for tf_{low}, tf_{medium}, and tf_{high} were applied to all experiments, and the resulting performances were compared. At the transition between the domains the filter combination for the binary matrix tf_{medium} had the best performance, so this filter combination was applied to both current densities $J = 0.5$ and $J = 2\,\mathrm{mA\,cm^{-2}}$ at the transition of the domains (see also Section 2.5).

2.4. The NNBA to Identify Pixel Clusters with Deposited Lithium

Artificial neural networks have already proven their value in a wide field of image-processing applications, and they have been shown to achieve better results than conventional computer algorithms.[19–24] Once designed, neural networks can generalize data from systems used during training, making them robust and universally applicable to unknown data sets. Therefore, an NNBA was developed as a second approach to identify deposited lithium on a Li metal surface.

The experiments had to be split into two sets for training and evaluation of the NNBA, respectively. For every current density, four out of five experiments were used to train the neural network, while the fifth experiment of every current density was used to analyze the performance of the NNBA. From each experiment, a reduced set of 12 images was selected to train the neural network. Image 1 showed the electrode before the CC phase, and this image was used as the initial state for every pixel in the identification process. Images 2–7 showed the evolution of deposited lithium during the CC phase, where images 2 and 7 were, respectively, the first and last recorded images. The almost equidistant intervals between these images were based on the number of recorded images during the CC phase. Images 8–12 were all recorded after the CC phase and had a time interval of 1 h between them. At first glance, images 7–12 showed an identical state for the deposited lithium on the electrode. However, minor pixel changes altered the character of the numeric image matrix, which made them ideal to train any noise in the images. Deposited lithium was then manually masked for each pixel in images 2–7. Each pixel in the image is assigned to either the object class true (pixel with deposited lithium) or false (all other cases).[25,26] The mask of the seventh image was applied to images 8–12 since the appearance of images 7–12 was almost identical. This approximation artificially increased the number of training data without increasing the human labeling workload. Hence, 36 experiments with 12 images each yielded a pixel-based manual masking of 432 images.

A convolutional neural network (CNN) was used as a basis for the NNBA, where input- and output-layer dimensions[27] were set to $366 \times 326 \times 1$. The center region in the images showed reflections from the opposite electrode, which resulted in significantly different brightness and contrast when compared to both two outer regions. The CNN could be trained more universally to detect deposited lithium under various conditions by including the center region and both outer regions as separate images in the training data. The pre-processed grayscale images with 1098×326 pixels (Figure 1d, blue rectangle) were cut into three equal-sized fragments (366×326 pixels). A consequence of this fragmentation is the increase of the number of masks from 432 (full-size images) to 1296 (432 images $\times$ 3 fragments). The schematic network design is shown in **Figure 3**.

The output of the identification process with a neural network is a matrix with the value 'true' for detected deposited lithium, which will be compared with the manually obtained masks. The number of convolution layers was set to 8 and the filter size to 25 (5×5) pixels to get the lowest number of misidentified pixels. The ReLU-function[28,29] was chosen as the neuron activation function. A stochastic gradient descent with momentum (SGDM) solver[30,31] was then used to train the network. A momentum of 0.9 and an initial learning rate of 0.001 were

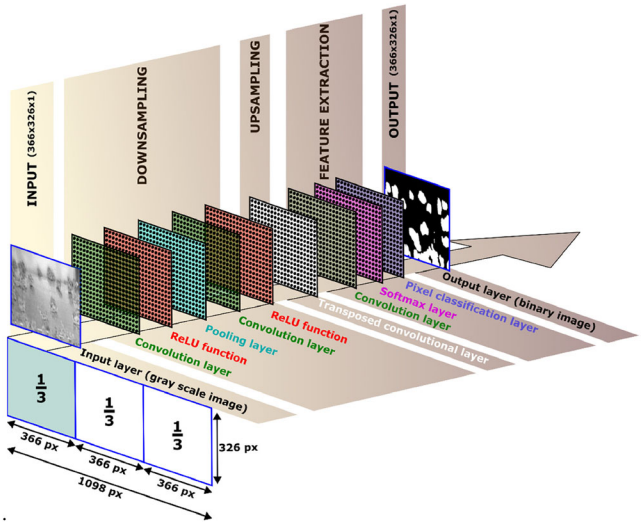

Figure 3. General network design of the convolutional neural network in the NNBA with an input layer, different layer types, and an output layer (from left to right).

chosen as parameters to ensure that the training algorithm converges to the loss functions' (cross-entropy loss) optimal value. With a mini-batch size of 64 images and 22 iterations per epoch, the accuracy of the network was stopped at 1000 epochs (S4).

Based on the findings of the RBA, additional filters were combined with the CNN to generate the NNBA. A morphological opening filter (*MorphOpen*) was calculated to improve the detection performance. Furthermore, a Frangi filter was applied on images 1–12 when the current density was smaller than $J = 5\ \mathrm{mA\,cm^{-2}}$. The Frangi filter was used to improve the detection of lamellar deposited Li structures, which were too difficult to detect by the CNN alone. The Frangi algorithm[32] was originally designed to detect blood vessels in the human body. Due to similar appearances between lamellar deposited Li structures and human blood vessels, the Frangi filter was found to be suitable for this case. The three filter types (CNN, morphological opening filter, and Frangi filter, see **Figure 4**) were combined with each other to obtain the binary matrix tf_{NNBA}

$$tf_{NNBA} = (tf_{\mathrm{CNN}} \,|\, tf_{\mathrm{MorphOpen}} \,|\, (tf_{\mathrm{Frangi}} \,\&\, \mathrm{J} < 5\ \mathrm{mA\,cm^{-2}})) \quad (5)$$

Furthermore, for every image in the series, the identified pixels in the initial state (image 1) were subtracted from identified pixels by the NNBA to minimize the likelihood of misinterpretations. The final image is then subjected to postprocessing procedures designed to remove noise, fill small gaps within the detected deposited lithium, and eliminate artefacts due to reflections and shadows, as described at the end of Section 2.6.

2.5. Performance Analysis of *RBA* and *NNBA*

The performance of both identification algorithms is analyzed by comparing the resulting binary matrix of the algorithm with the manually masked image at the end of the CC phase. The manually masked images (Figure 1d) were converted into binary matrices. Pixels that were identified as deposited lithium were assigned the value 'true,' and all other pixels were assigned the value 'false'. A pixel-by-pixel comparisons (**Figure 5**b) can have one of four possible classifications in a confusion matrix: true positive (*tp*), false positive (*fp*), false negative (*fn*), and true negative (*tn*).[33,34] Only pixels on the electrode plateau (yellow area in Figure 1d) were evaluated for the performance analysis. The performance of both automated approaches was quantified with the statistical metrics precision P,[33,35] recall R,[33,35] and F_1-score.[33,35–38] These metrics are defined as

$$P = \frac{\sum tp}{\sum tp + \sum fp},\ R = \frac{\sum tp}{\sum tp + \sum fn} \text{ and } F_1 = 2 \cdot \frac{P \cdot R}{P + R} \quad (6)$$

Results of the performance analysis of the *RBA* confirmed that transitions between domains with low or high current densities and the transition region are not ambiguous. In previously published work[8] the transition at $J = 0.5\ \mathrm{mA\,cm^{-2}}$ was assigned to low current densities, and the transition at $J = 2\ \mathrm{mA\,cm^{-2}}$ was assigned to high current densities, which complied with electro-chemical and optical data. Figure 5a shows an example of deposited lithium at the end of the CC-phase for a current density equal to $J = 2\ \mathrm{mA\,cm^{-2}}$ (i.e., transition between medium and high current densities). Application of the RBA binary matrix tf_{high} for high current densities resulted in false identification of almost the whole electrode area as pixels with deposited lithium (see Figure 5c). On the other hand, the application of the RBA binary matrix tf_{medium} for medium current densities produced a far more realistic result (see Figure 5d). So, different domain transitions are obtained from automated image processing when compared to results from electrochemical or optical data.

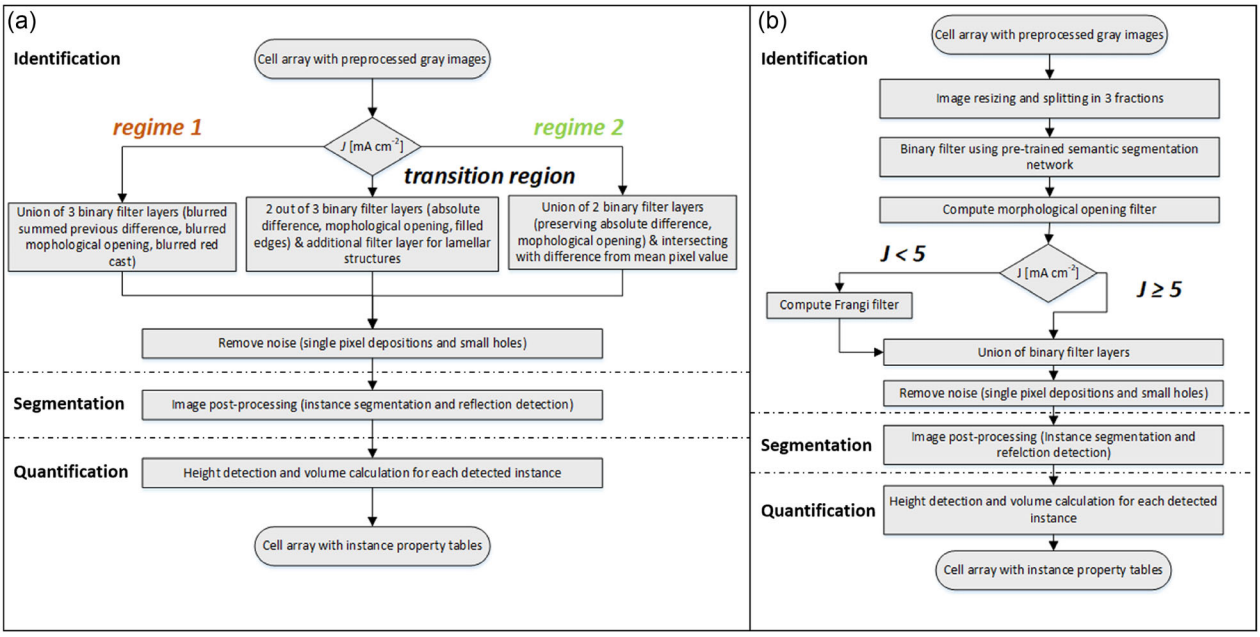

Figure 4. Schematic workflows of a) rule-based approach (RBA) and b) neural network-based approach (NNBA).

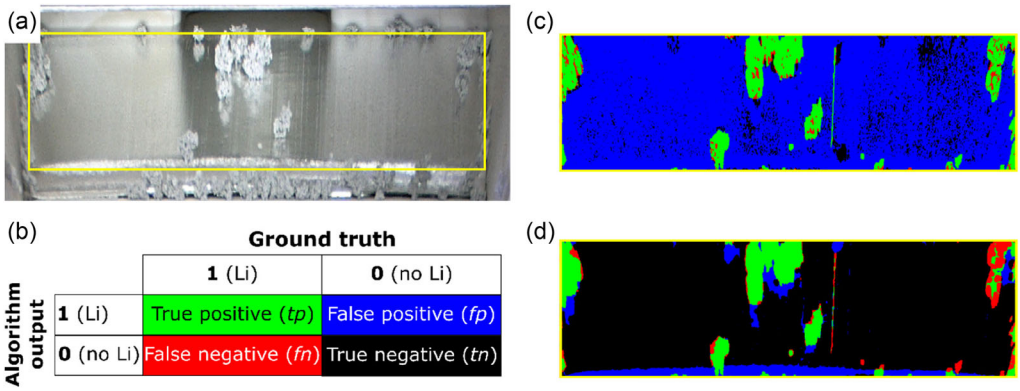

Figure 5. Example of deposited Li structures at $J = 2$ mA cm^{-2}. a) Preprocessed RGB image at the end of the CC phase. b) Confusion matrix with four possible outcomes to assess the identification process. c) Values from the confusion matrix of pixel-based identification process when tf_{high} is applied for *RBA*. d) Values from confusion matrix of pixel-based identification process when tf_{medium} is applied for *RBA*.

Figure 2 compares the F_1-scores of the identification process for RBA, NNBA, and masking by a second person, where the masking by the first person was always the reference. All three approaches have a similar trend: acceptable F_1-scores at low current densities which increase to good F_1-scores at high current densities. In general, the F_1-score of the NNBA was better than the F_1-score of the RBA. Both identification algorithms were optimized or trained using the pixel-based manual masks, and both approaches did not reach a F_1-score of 100%. Furthermore, a comparison of masking by two different persons did not result in a F_1-score of 100%, but interestingly the trend of the F_1-score for all approaches was very similar. This shows very clearly how challenging it is to identify deposited lithium on Li metal.

The lowest current density of $J = 0.05$ mA cm^{-2} has the lowest F_1-score. The reason for the low score can be attributed to the presence of tiny, deposited Li structures, which were challenging to be detected. The noise level in the images is of the same order of magnitude as any variation due to deposited lithium. Variations in gray scales due to noise might be identified by the RBA as deposited lithium and result in the creation of seed points. The NNBA also identified tiny, deposited Li structures on the electrode surface that are not visible to the human eye.

Table S6, Supporting Information, shows the complete statistical metrics (mean values for precision, sensitivity, and F1-score). Note that those values include all experiments for the RBA and only the evaluation experiments for the NNBA since the training data sets would be biased.

2.6. Segmentation of Pixel Clusters into Instances of Deposited Lithium

Both identification algorithms identify seed points of the deposited lithium during the CC phase. Clusters of deposited lithium grew into larger clusters or agglomerations of clusters when the charge was transferred. These automatically detected clusters of deposited lithium must be separated into individual instances of deposited Li structures based on their seed points (**Figure 6**). Single instances can be detected when two structures have sufficient space between them. In most cases, a watershed algorithm[37] would allow a proper instance segmentation, but here the porous morphology of deposited Li structures and the missing borderlines made it impossible to separate them with such an approach.

Thus, another instance segmentation process is implemented as part of the postprocessing. Separation of deposited Li-structures into instances is based on the coordinates of detected seed points, which are the centroid coordinates of the first appearance of deposited Li structures on an electrode surface from previous images in the recorded series. Two binary matrices were generated from the previous image (Figure 6b): the first binary matrix contained all instances larger than or equal to 30 consecutive pixels (tf_{large}) and the second binary matrix contained all instances smaller than 30 consecutive pixels (tf_{small}). The threshold of 30 pixels was selected to prevent excessive segmentation due to image noise.

In the next step, a morphological thickening process is performed on the binary matrix tf_{large}. This results in a binary matrix $tf_{SkelImage}$ that is everywhere equal to 'true', except for a 1-pixel wide band with the value 'false' in the middle of boundary surfaces of instances (Figure 6c). This process keeps the total number of instances and holes in these instances constant (Euler number[38]). The final step computes an instance-separated image with a logical combination of three binary matrices (Figure 6d).

$$tf_{segment} = tf_{large} \;\&\; (tf_{SkelImage} \mid tf_{small}) \tag{7}$$

This logical combination results in a binary matrix where instances larger than or equal to 30 consecutive pixels from previous images will be separated while smaller instances stay intact (Figure 6e).

Deposited Li structures can grow as large and bulky instances (especially at medium current densities). This results in reflections of deposited Li structures on the electrode surface, which are likely to be falsely identified as deposited lithium. Multiple attempts to prevent these false identifications by pixel-based algorithms have not been successful, so an alternative approach has been implemented. It is very unlikely that the growth of an instance will be directed towards the lower edge of the electrode (Figure 1a, 'bottom'-side). Changes in the center of mass of instances can be calculated by comparing centroid coordinates in the current image with centroid coordinates from previous images. If this change is towards the lower edge of the electrode

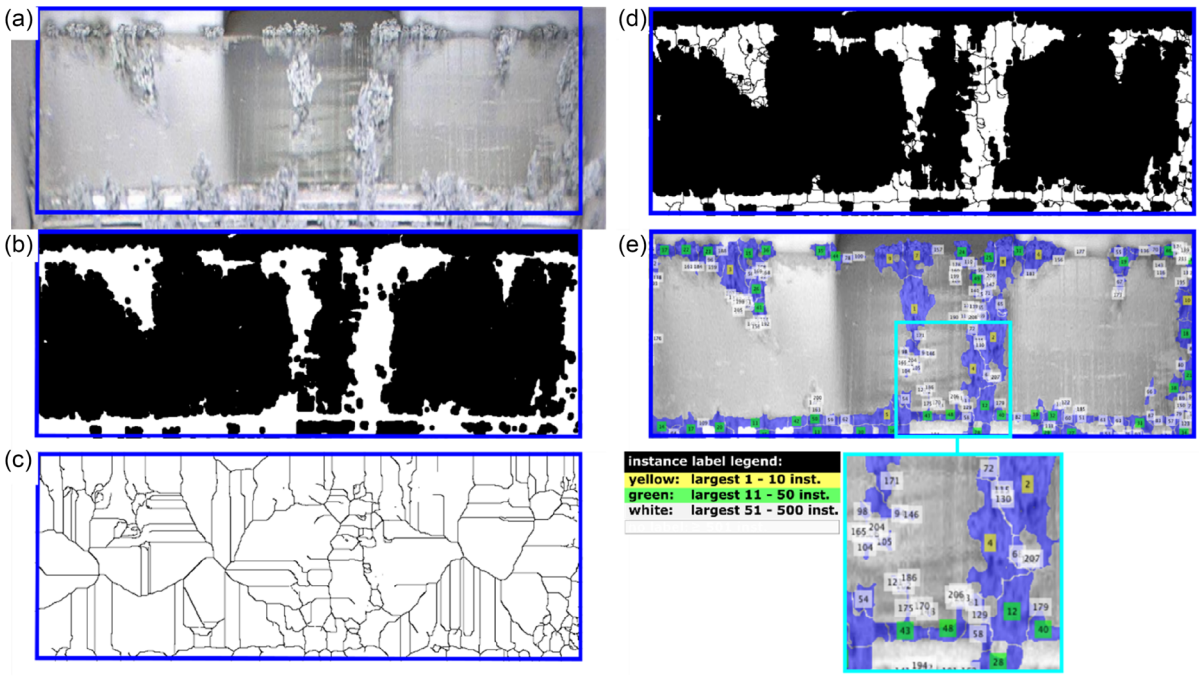

Figure 6. Example of instance segmentation process for *RBA* at $J = 1\ \mathrm{mA\,cm^{-2}}$: a) Original image. Blue rectangle: area where instances are segmented (see also Figure 1). b) Binary matrix obtained with *RBA* identification algorithm with deposited lithium (white pixels) and all other cases (black pixels). c) Segmentation pattern of growing instances based on individual seed point coordinates. d) Segmentation of pixel clusters by combining (c) with (b). e) Full view and zoom view of segmented Li deposition structures with corresponding instance labels.

and the instance has a detectable size, then it can be identified as a reflection. The reflective part of an instance can be determined by a shape comparison between its first appearance and the current image in the series, and the corresponding pixels can be removed from the instance.

3. Automatic Quantification of Deposited Lithium

After segmentation of the deposited lithium, individual instances of deposited Li structures could be quantified as a function of current density. For instance, the number of instances N could be counted, or a characteristic length scale L could be determined for every instance. Based on these two parameters, the volume of every instance V_{inst} could be approximated and then summed to obtain the total volume V_{total} of deposited lithium. These quantifications were automatically evaluated for both RBA and NNBA. Additionally, N and L are also compared with the results of the MEA. The fourth section will discuss the time evolution of the total deposited volume, where the normalized charge throughput will be used as a time scale. The impact of the sampling rate on the performance of the automated image processing is shown and discussed in the fifth section. Note that the algorithms are applied to images from previous work, where there were some issues with different ageing of the lithium foils (As stated in a previous study,[8] the Li deposition experiments were unintentionally conducted with two 'types' of Li foils. Li foil from the same manufacturer and production batch was used. However, the ordered amount of lithium was distributed over two pouch bags, which were used one after another. The first set of experiments was conducted with lithium from the first pouch bag ($J = 0.1\ \mathrm{mA\,cm^{-2}}$: 5/5 experiments, $J = 1\ \mathrm{mA\,cm^{-2}}$: 5/5 experiments, $J = 10\ \mathrm{mA\,cm^{-2}}$: 1/5 experiments), then the remaining experiments were conducted with Li foil from the second pouch bag ($J = 10\ \mathrm{mA\,cm^{-2}}$: 4/5 experiments, all remaining current densities). Based on the electro-chemical and optical data, it became clear that the Li foils experienced different aging although they were stored under inert gas conditions (Ar-atmosphere, $H_2O < 1$ ppm, $O_2 < 1$ ppm). This was observed after all 45 experiments (9 current densities × 5 experiments) were conducted. No electro-chemical evaluation is performed in this work, instead automated image processing algorithms are developed and assessed. Consequently, all recorded experiments were used in this work to assess the automated algorithms). While the aging effects had a strong impact on the electrochemical impedance of the electrode foils, the deposition behavior did not seem to be impacted significantly. For increased reproducibility of Li metal-based experiments, we would recommend storing Li foil in a vacuum chamber connected to a glovebox instead of in the glovebox itself. Additionally, performing a standardized electrochemical test with the comparable setup conditions using electrochemical impedance spectroscopy or a similar method is suggested to verify if the Li foil still shows the same conditions as before. Another experimental approach, presented by Rospars et al., uses a vacuum thermal evaporation method to produce Li metal foil with a highly pure surface and a thinner natural passivation layer.[39] Producing the Li foil with this method before each experiment should minimize lithium foil aging-induced deviations.

3.1. Number of Instances

The first property to quantify deposited lithium is the number of instances N detected in a single image at the end of the CC phase. **Figure 7** shows the mean number of instances $\overline{N}$ of all five experiments as a function of current density J, as they were detected with the RBA and NNBA, respectively. For the RBA, the mean number of instances $\overline{N}$ increases at lower current densities and stays nearly constant for medium current densities. The trend for the number of instances determined with NNBA does, in general, resemble the trend of the RBA. The major deviation between both approaches is at a current density of $J = 10\,\mathrm{mA\,cm^{-2}}$, where $\overline{N}$ is significantly lower for the NNBA. This might be attributed to the large charge throughput between two recorded images (see also Section 3.5), which resulted in a small number of initial seed points that could be detected in the first image after the start of the CC phase (image 3). Detection and separation of individual instances works better when more images are provided for the same charge throughput. In addition, the NNBA tends to identify additional false positive pixels around small instances because the convolution layer causes smearing of peripheral areas, resulting in additional connections of seed points that are close together. This is the reason why the NNBA instance segmentation underperformed for the highest current density. The filter designed for high current densities in the RBA was able to detect most instances in the first image after the start of the CC phase.

In the case of the MEA, a human expert manually counted all individual instances. Only instances larger than $L = 0.2$ mm were counted for current densities smaller than $J = 2\,\mathrm{mA\,cm^{-2}}$. The number of instances for current densities larger than $J = 5\,\mathrm{mA\,cm^{-2}}$ had to be approximated due to the huge number of deposited Li structures. Instances were counted on a small portion of the electrode, which would then be upscaled for the complete electrode area. This procedure carries a risk of selective data inclusion, which might explain the discrepancy observed between the MEA and the two automated approaches. For both the RBA and NNBA, the number of instances corresponds to the number of identified seed points of all experiments in the full range of current densities.

It can be concluded that there were significant differences in the number of instances N for the various approaches. The MEA disregarded all tiny instances, while both automated approaches registered all sizes of instances. At the highest current densities, inaccuracies might be caused in the MEA due to so-called cherry picking and for the NNBA due to a too large charge throughput between two recorded images.

3.2. Characteristic Length Scales of Instances

The circumferential diameter can be used as a characteristic length scale L of each individual instance. It will be used as the second property to quantify lithium deposition in this work. The mean characteristic length scale $\overline{L}$ is determined as the arithmetic mean value of every instance detected in the images of all five experiments for a given current density. **Figure 8** shows the determined mean characteristic length scale $\overline{L}$ as a function of current density J for both automated approaches and the MEA. Both automated approaches used the MATLAB *regionprops*-function to determine the characteristic length scale of each individual instance.

In the case of the RBA, the mean characteristic length scale $\overline{L}$increases from low current densities to a maximum around a current density of $J = 2\,\mathrm{mA\,cm^{-2}}$. For current densities larger than $J = 2\,\mathrm{mA\,cm^{-2}}$, the length scale decreases to the point

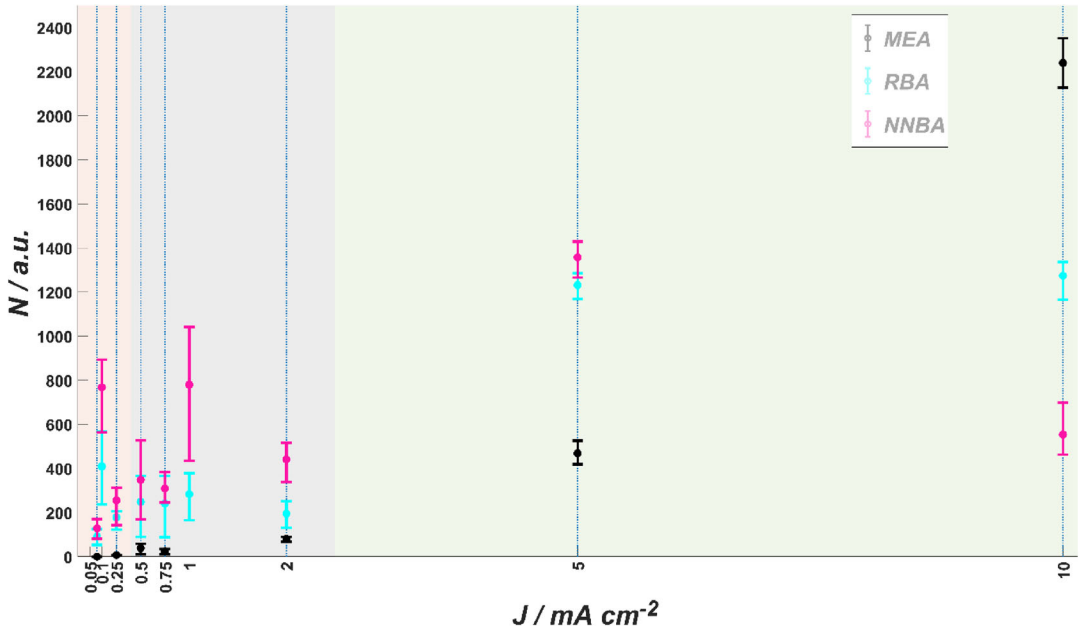

Figure 7. Number of instances N of deposited Li-structures as a function of current density J determined with the RBA, NNBA and MEA. The dots are the mean values and the given error bars represent the 25%- and 75%-quantiles.

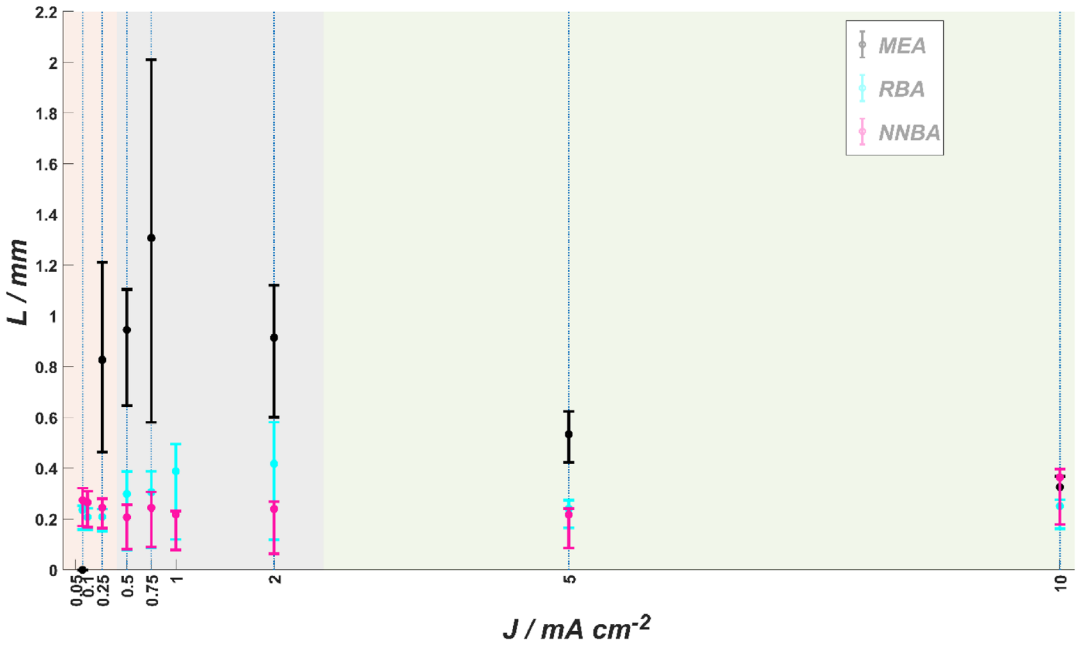

Figure 8. Determined characteristic length scales L of instances of deposited Li structures as a function of current density J for both automated approaches and the *MEA*. The dots are the mean values, and the given error bars represent the 25% and 75% quantiles.

where the lowest and highest current density of the complete range obtained similar values.

At low current densities $J < 0.25$ mA cm^{-2}, the mean characteristic length scales $\overline{L}$ detected by NNBA are slightly larger than those of the RBA or MEA. The NNBA proved to be significantly more sensitive to detecting potentially deposited lithium and therefore identified larger structures at lower current densities. At low current densities, the duration of the experiment is so long that passivation reactions on the surface or changes in environmental conditions might lead to severe changes in the image, that are not triggered by the charge throughput (Li-deposition process), eventually leading to misinterpretations in the image evaluation. For higher current densities, the large charge throughput between two recorded images results in irregular, extensive clustering of deposited Li structures that cannot be separated by the segmentation algorithm (see also Section 3.5). The NNBA does not show a clear maximum at medium current densities, which is a distinction compared to RBA and MEA. It should be noted that for the NNBA, only one single neural network is responsible for the pixel-wise identification. Besides the correct recognition of the deposited Li structures, an interference-free image sequence is also necessary for the error-free segmentation into instances. The manual masks should also include information on the instance boundaries to improve the robustness of the instance-based evaluations.

Note that the MEA has been performed on the trapezoidal raw image (see Figure 1c), which leads to a position-dependent distortion of the size of Li structures on the electrode surface. For better comparability with the MEA results, the length scales of single instances of both automated approaches in Figure 8 were purposely retransformed to trapezoidal raw images.

3.3. Approximated Total Volume of Instances

The ultimate objective for the quantification of deposited lithium is to determine the total deposited volume V_{total} at the end of the CC phase. Accurate estimations for the total volume of deposited lithium are only feasible with automated approaches because each instance of a deposited Li structure must be assessed individually. One of the main challenges is to obtain 3D information from 2D images, which requires some kind of geometrical modelling. The circumferential shape of instances of deposited Li structures can be approximated by various geometries such as spheres, ellipsoids, or rotational bodies. **Figure 9**a shows an example of a high-resolution close-up image of an instance, which was recorded at the end of an experiment with a 100x magnification and a recording angle of 5°. This image will be used to explain three approximations analyzed in this work.

The first approximation considered all instances to be spheres (Figure 9b). It is assumed that the diameter is equal to the characteristic length scale L determined in Section 3.2 to determine the spherical volume V_{sphere}. The characteristic length scale is converted into mm units using the scale from the microscope shown on the images. The major drawback of this approach is that not all instances have a spherical shape, which causes relatively large errors in the volume approximation.

The second approximation considered every instance as an ellipsoid (Figure 9c). The volume of an ellipsoid $V_{\text{ellipsoid}}$ is determined by three axes: major axis, minor axis, and height. An automated image processing can automatically determine the major and minor axes (length and width) of each instance individually. The height of an instance is defined as the distance from the seed point to the top of the bounding box of the instance. For branched instances (instance area $<$ 0.1 * bounding box area),

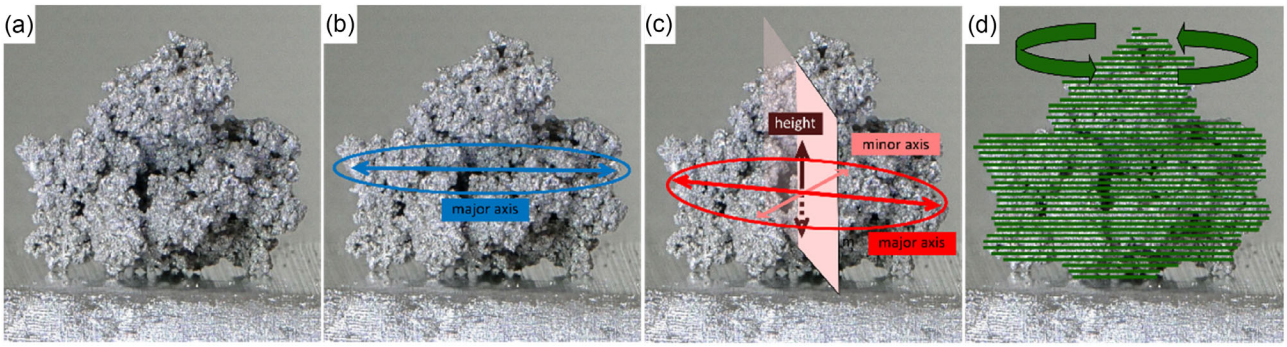

Figure 9. Various geometrical approximations for the volume of instances V_{inst} of deposited Li structures. a) Image of example instance (100x magnification, 5° recording angle). b) Instance volumes are approximated as spheres using a characteristic length scale. c) Instance volumes are approximated as ellipsoids with major axis (largest diameter), minor axis (orthogonally to major axis), and height (orthogonal to major-minor plane). d) Instance volumes are approximated as rotational bodies (rotation of 1-pixel wide stripes orthogonal to the instance growth axis).

the instance height is set equal to the minor axis. The instance area is defined by the number of pixels that are assigned to this instance, while the bounding box is the smallest rectangle using only horizontal and vertical lines that can include the instance. The advantage of this method over the spherical approximation is that nonspherical instances can be estimated with higher accuracy.

The third approximation considered each instance of a deposited Li structure as a fully rotational geometry (Figure 9d). Each 2D plane in the image was segmented into 1-pixel-wide thin stripes, such that a rotational 3D body can be generated by rotating the strip around an axis in the plane of the image. This is done by calculating the volume of every strip, where the diameter of each strip equals the corresponding length. Finally, all strips are summed to obtain the volume $V_{rotation}$ of the rotational body. With this method, the volume of any geometrical shape can be approximated with higher accuracy.

Table 2 compares the geometrical approximations to determine the mean instance volumes of deposited Li structures $\overline{V}_{inst}$ at various current densities. The mean value is determined as the arithmetic mean value of every instance in the five images for a given current density. There are two conclusions based on this table. First, the volumes of the spherical model can be an order of magnitude 10 times larger than both the ellipsoid model and the model of rotational bodies. This shows the huge disadvantage of this approach when the instances do not have a spherical shape. Secondly, the ellipsoid model and the model of rotational bodies result in the same range of instance volumes. For the remainder of this work, the model of rotational bodies will be used to approximate the instance volumes.

The next step is to determine the total volume V_{total} of the deposited lithium, which is calculated as the sum over the volumes of each individual instance V_{inst} in one experiment. The mean total volume $\overline{V}_{total}$ is then obtained by calculating the arithmetic mean value of the five experiments corresponding to one current density. There are two things to be considered for the assessment of the total volume. First, part of the Li metal could be deposited as a thin, homogeneous, planar layer on top of the surface of the Li metal instead of clearly visible Li-structures. This layer might not be optically visible, and it can then not be detected by the automated approaches. Secondly, based on the total charge throughput of $Q_{total} = 10.9$ mAh, it is possible to calculate the theoretical maximum volume that can be deposited as $V_{max} = 5.3\ mm^3$ considering the deposition consists only of pure Li metal without any porosity. Experimental studies using SEM-EDX, Raman, mass spectrometry, and XRD[40,41] have shown that the Li metal foils and especially the deposited structures do not consist only of Li metal but also potentially of decomposition species, e.g., such as lithium carbide species like Li_2C_2. If all lithium that is reduced would be deposited as lithium carbide, the theoretical maximum volume of lithium carbide can be deposited as $V_{max} = 5.9\ mm^3$. This number is therefore only

Table 2. Comparison of geometrical models to approximate the mean volume of instances of deposited Li structures $\overline{V}_{inst}$ in mm^3.

		Current density [mA cm^{-2}]								
		0.05	0.1	0.25	0.5	0.75	1	2	5	10
V_{sphere}	RBA	0.35	0.018	0.035	0.32	0.31	0.51	0.63	0.041	0.27
	NNBA	0.092	0.046	0.036	0.17	0.16	0.15	0.21	0.35	2.2
$V_{ellipsoid}$	RBA	0.0012	0.00093	0.00095	0.012	0.010	0.014	0.036	0.0038	0.004
	NNBA	0.00011	0.00045	0.00020	0.0019	0.0034	0.0069	0.023	0.0064	0.026
$V_{rotation}$	RBA	0.0016	0.0013	0.0013	0.016	0.011	0.014	0.043	0.004	0.0047
	NNBA	0.00012	0.00052	0.00022	0.0011	0.0026	0.0048	0.015	0.0077	0.025

11% higher than the deposition of Li metal, and the order of magnitude remains valid for the reference value.

The dots in **Figure 10** show the detected mean total volume $\overline{V}_{total}$ of deposited Li structures for various current densities. At low current densities, the detected and deposited volume is relatively small (orange background), which indicates that part of the Li metal might be deposited as a thin, homogeneous, planar layer on top of the surface. At high current densities (green background), the volume has the order of magnitude of the theoretical maximum volume, so for high current densities, most of the lithium is deposited as clearly visible structures. The total volume can be larger than the theoretical maximum value because the deposited Li structures have a porous morphology. The *RBA* has a sudden increase around a current density of $J = 0.5\ \mathrm{mA\,cm^{-2}}$ and fluctuates around the theoretical maximum value for increasing current densities with a relatively stable uncertainty. Interestingly, the largest volume is at a current density of $J = 2\ \mathrm{mA\,cm^{-2}}$, which complies with the largest characteristic length scale in Figure 8. The *NNBA* has a smooth gradual increase of the total volume with increasing current densities, which is accompanied with an increasing uncertainty in the total volume. This intriguing result shows the power of this approach, since neither the number of instances nor the characteristic length scale showed such a clear trend (see Figures 7 and 8). At low and medium current densities, there is good agreement between both automated approaches, except for the transition between those regions (viz., $0.5 \leq J \leq 0.75\ \mathrm{mA\,cm^{-2}}$). At high current densities, the *NNBA* has detected a larger total volume than the *RBA*, which might be due to difficulties in the segmentation process in the *NNBA* (see Section 3.5).

A direct comparison between the *MEA* and both automated approaches is not feasible for the total deposited volume. For the automated approaches, preprocessing is applied (see Section 2.2) that cannot be repeated in a manual process. Furthermore, for *MEA*, only an assessment with the spherical approximation is feasible, but this section has shown that this geometrical model produces large errors.

3.4. Time Evolution of Total Deposited Volume

Automated approaches enable a time-resolved evaluation of deposited lithium by assessing time sequences of images during the CC phase. **Figure 11** shows such an assessment for the lowest current density at $J = 0.5\ \mathrm{mA\,cm^{-2}}$ and the highest current density at $J = 10\ \mathrm{mA\,cm^{-2}}$, which were evaluated for both the *RBA* and the *NNBA*. The total deposited volume V was based on the approximation with rotational bodies and is normalized as $v = V/V_{total}$, where V_{total} is the respective value at the end of the CC phase. Time was plotted as normalized charge throughput $q = Q/Q_{total}$, where $Q_{total} = 10.9\ \mathrm{mAh}$.

In the case of the lower current density $J = 0.5\ \mathrm{mA\,cm^{-2}}$, the evolution of total deposited volume showed for both automated approaches an asymptotic behavior towards a linear curve. Both automated approaches showed a more logistic growth behavior for the highest current density $J = 10\ \mathrm{mA\,cm^{-2}}$. At the start of the CC phase, numerous small instances were formed, which led to a significant increase in total deposited volume within the first $q = 20\%$ of the CC phase. Then, individual instances continued to grow, which led to a further increase of the total deposited volume at a lower rate of increase.

The fluctuations in the evolution resulted from the iterative image evaluation of the approaches. For each individual image of the CC phase, firstly, the pixels were identified that showed deposited Li structure. In a second step, the identified pixel clusters were separated into instances, then for every individual

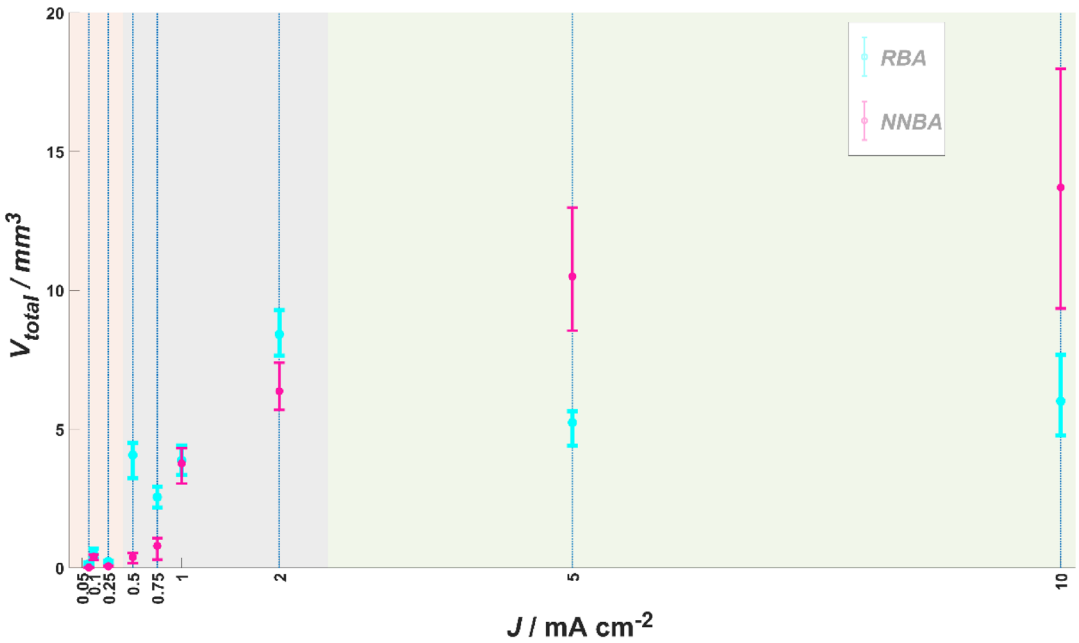

Figure 10. Total volume V_{total} of deposited Li structures as a function of current density J for both automated approaches. Volumes are approximated as rotational bodies, the dots are the mean values, and the given error bars represent the 25% and 75% quantiles.

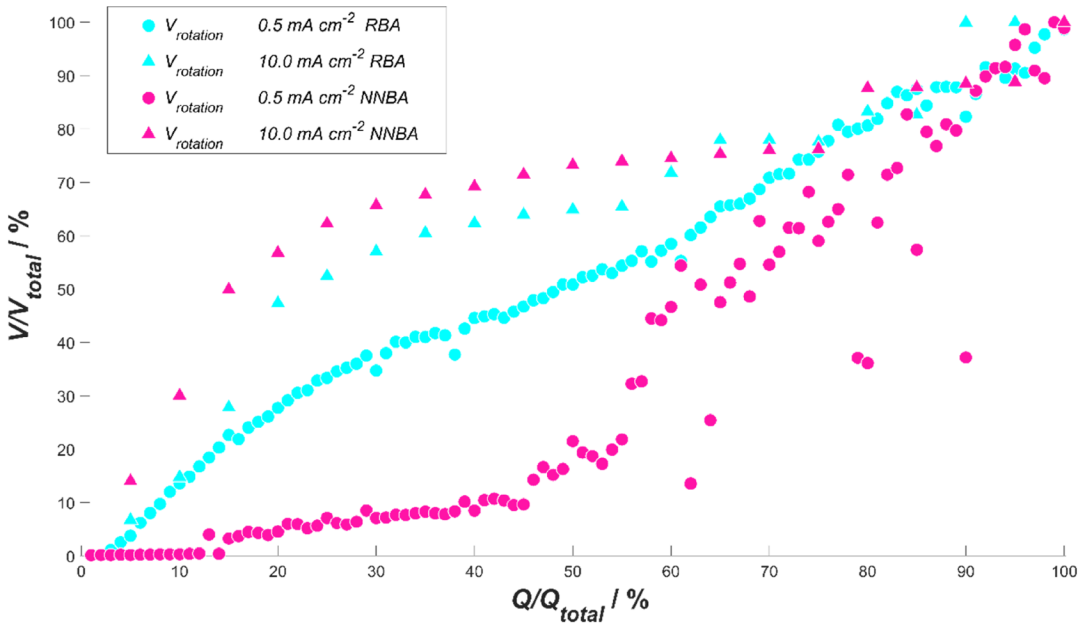

Figure 11. Example of time evolution of normalized deposited volume $v = V/V_{\text{total}}$, where the normalized charge throughput $q = Q/Q_{\text{total}}$ is used as a measure for time.

instance the rotational volume V_{inst} was calculated, and these rotational volumes were summed to determine the total deposited volume V. Growth of instances during the charge transfer changed the dimensions, contrast, light conditions, and shadows. Since each image in the series is reevaluated on its own for the NNBA, there might be discontinuities in the identification of deposited Li structures and the segmentation into instances.

3.5. Influence of Sampling Rate on Automated Image Evaluation

It has been mentioned in previous sections that the algorithm to determine characteristic length scales and instance volume for both RBA and NNBA is not accurate at high current densities. This might be due to the large charge throughput of $Q_{\text{eval}} = 545\ \mu\text{Ah}$ between two recorded images, such that too much is changing between two images. It was assumed that the performance of the segmentation algorithm would improve when more images would be available (and consequently there would be less between the images). An auxiliary experiment was performed at the highest current density equal to $J = 10\ \text{mA cm}^{-2}$ with a reduced time interval of $t_{\text{sample}} = 1\ \text{s}$ between two recorded images to test this hypothesis. The reduced time interval resulted in $N_{\text{sample}} = 300$ images and a corresponding charge throughput of $Q_{\text{eval}} = 36.3\ \mu\text{Ah}$ (see also Table 1). Recall that the first image of the CC phase is recorded after the charge is transferred, so the number of images is equal to the number of intervals.

It was necessary to use an auto clicker tool (OP Auto Clicker, Copyright 2022, opautoclicker.com. All Rights Reserved) to enable a lower sample interval because the KEYENCE software of the digital microscope did not allow sample intervals smaller than $t_{\text{sample}} = 15\ \text{s}$. A second series of images were artificially generated by deleting images such that $N_{\text{sample}} = 20$ images, sample interval $t_{\text{sample}} = 15\ \text{s}$, and $Q_{\text{eval}} = 545\ \mu\text{Ah}$ were obtained (see **Table 3**).

Both the *RBA* and the *NNBA* were applied to both series of images and then compared with the manually obtained mask of the last image in the CC phase to evaluate the performance of the pixel-wise identification algorithm. The resulting four sets of statistical metrics were used to assess the influence of the charge throughput Q_{eval} between two images on the performance of the pixel-wise identification algorithm. The identification algorithm of the *RBA* does depend on the charge throughput Q_{eval} between two recorded images. The *SummedDiff* filter (Section 2.3, high current densities) creates a union of all identified pixels from the previous images. Due to the large number of images in this experiment, the filter was oversensitive and detected each pixel as deposited lithium. This output is confirmed by a manual evaluation of the auxiliary experiment by

Table 3. Performance of the RBA and NNBA for an auxiliary experiment at $J = 10\ \text{mA cm}^{-2}$ with two different sample rates for the recorded images (precision P, recall R, and F_1-score).

		RBA			NNBA		
Pixel-wise identification algorithm							
N_{sample}	Q_{eval} [μAh]	P [%]	R [%]	F_1 [%]	P [%]	R [%]	F_1 [%]
20	545	97	59	73	98	91	94
300	36.3	97	100	98	98	91	94
Segmentation algorithm							
N_{sample}	Q_{eval} [μAh]		N			N	
20	545		1255			728	
300	36.3		1654			1303	

the human expert, who identified 97% of the electrode area as deposited Li structures in the pixel-based manual masking (see precision P in Table 3). Reduction of the charge throughput Q_{eval} did not result in any measurable change in the performance of the pixel-wise identification algorithm in the case of the *NNBA*. Table 3 shows both sample rates the F_1-score, which were identical with a value of 94%. The identification algorithm of the *NNBA* is independent of the time interval between recorded images because it does not rely on pixel changes between the current and previous image.

The bottom rows in Table 3 show for four cases the number of instances N that were detected with the segmentation algorithm. For both automated approaches, there was a significant increase in the number of detected instances when the charge throughput Q_{eval} between two recorded images was reduced. By recording more images, there was less charge throughput between two images, such that the seed point formation prior to the actual growth of deposited Li structures could be detected more selectively and unwanted clustering could be avoided.

Both automated approaches detected a low number of instances, when the charge throughput between two images was equal to $Q_{eval} = 545\ \mu Ah$ (see Figure 7). The number of detected instances N matches better with the MEA in the case of a lower charge throughput $Q_{eval} = 26.33\ \mu Ah$. When more images per charge throughput are available for the automated approaches, instances can be detected earlier, which facilitates instance segmentation. In conclusion, for optimal instance detection, the charge throughput Q_{eval} between two images should be low enough to detect each individual seed point and should be identical for all current densities. Therefore, the charge throughput Q_{eval} between two images should be determined by the highest current density (which has the fastest processes in this set of experiments).

4. Conclusion

Previous work by the authors showed how optically accessible cells could be a valuable tool to study the lithium deposition behavior on Li metal. A recurring challenge in such approaches is to automatically quantify the amount of deposited lithium based on the obtained images, which is precisely the objective of this work. Manual masking of images by two different persons resulted in far-from-perfect F_1-scores, and this observation confirmed the challenging nature of developing such a workflow.

The workflow consisted of the following three major algorithms: pixel-wise identification of deposited lithium, segmentation of pixel clusters into instances of deposited Li-structures, and instance-based quantification of the amount of deposited lithium. Two methods to automatically identify pixels with deposited lithium have been developed: RBA and NNBA. The performance of both identification algorithms was analyzed by comparing the obtained binary matrices with manually generated masks. The determined F_1-scores of RBA, NNBA, and masking by second person had similar trends, although the NNBA had a better score than the RBA. Manually generated masks were used to calibrate filters or train the neural network in the automated approaches. The low-to-medium and medium-to-high current density transitions identified in this work did not completely comply with the optical findings of the previous work.[8] These differences show that the results are sensitive to the chosen image evaluation approach.

The segmentation algorithm enabled the instance-based characterization of deposited Li structures: number, characteristic length scales, and volume of deposited instances. There were clear distinctions in the number of instances determined by the MEA, RBA, and NNBA. At low current densities, there were almost no instances for MEA and a noticeable number for both automated approaches. At high current densities, there was an exponential growth in the number of instances for the MEA, where the automated approaches showed a more logistic growth behavior toward larger current densities. Both automated approaches did not show the clear maximum in the characteristic length scale at medium current densities as was shown by the MEA. Instances of deposited Li structures were approximated by three geometrical models to determine the volume: spheres, ellipsoids, and rotational bodies. Instances of deposited Li structures do not have a spherical shape, so the circumferential spherical model resulted in large errors for the determination of the instance volume. Geometrical models based on ellipsoids and rotational bodies resulted in comparable instance volumes. Determination of the total deposited volume is only feasible due to the automated processing in RBA and NNBA. The determined total deposited volume at low current densities indicates that lithium is deposited as a thin, homogeneous, planar layer on top of the Li metal surface. At high current densities, the determined total volume of deposited lithium is of the order of magnitude of the theoretical maximum volume. Furthermore, both automated approaches enabled to assess the time evolution of deposited lithium volume and show different behaviors at low and high current densities. Finally, for high current densities, the amount of charge throughput between two recorded images can be too large to detect the seed points correctly, which causes issues with the segmentation algorithm.

5. Outlook

In this study, a single-carbonate-based electrolyte was used, and the current rate dependency was evaluated. Recent studies with Li metal showed highly improved performance using ether-based electrolytes, localized high-concentration electrolytes, and liquefied gas.[42] Future studies should therefore use the methods proposed in this work to evaluate differences in the Li metal deposition when using other electrolytes that have less electrolyte degradation and higher lithium deposition reversibility.

The observation of successive deposition and stripping of the Li metal should also be considered in future work to understand the formation of dead lithium[43–45] in different electrolytes. The setup used in this study does not use a separator or solid electrolyte to apply pressure to the Li metal surface. Figure S16, Supporting Information, shows that structures can therefore easily break off during deposition. Stripping the deposited Li metal resulted in most of the structures breaking off rapidly. This needs to be considered for future experimental designs.

During the manual evaluation of the image data, it seemed that the lithium depositions are more favorable to happen on the edges of the foil than on the center part. To quantify this, the site dependency of Li deposition as a function of current density was systematically evaluated using heat maps and binary

quantification grids (see Figure S17, Supporting Information). The results show that at low and medium current densities, Li preferentially deposits at the electrode edges, while at higher current densities, deposition becomes more uniform across the entire electrode surface. Quantitative analysis (Table S18, Supporting Information) reveals that the selectivity for edge deposition is most pronounced at certain intermediate current densities, but diminishes as current density increases, leading to nearly site-independent deposition at the highest values. These findings highlight a measurable correlation between current density and the spatial distribution of Li deposition, suggesting that electrode geometry and surface-to-edge ratio may further influence this behavior. Experimental setups for future studies should therefore try to mask the edges of the electrode to hinder lithium deposition at those sites.

Supporting Information

Supporting Information is available from the Wiley Online Library or from the author.

Acknowledgements

H.K. and S.B. contributed equally to this work. The authors thank the BMW Group for their financial support of this study. This project received also funding from the European Union's Horizon 2020 research and innovation program under grant agreement no. 769929. Furthermore, the authors thank Prof. Dr. Stegmaier and Dr. Strauch (Institute of Imaging & Computer Vision (LFB), RWTH Aachen University) for their valuable advice, which helped to design and optimize the RBA and NNBA. The authors further thank Dr. Akihiro Yamashita and Thorsten Tegetmeyer-Kleine for the valuable discussions and proofreading.

Open Access funding enabled and organized by Projekt DEAL.

Conflict of Interest

The authors declare no conflicts of interest.

Data Availability Statement

The data that support the findings of this study are available from [BMW - Dr Edwin Knobbe]. Restrictions apply to the availability of these data, which were used under license for this study. Data are available from the authors with the permission of [BMW - Dr Edwin Knobbe].

Keywords

electrochemistry, image evaluations, liquid electrolytes, lithium, material sciences

Received: February 24, 2025
Revised: June 5, 2025
Published online: July 13, 2025

[1] E. C. Evarts, *Nature* **2015**, *526*, S93.
[2] P. Y. Zhao, Y. Li, S. J. Chen, H. Fan, Y. Y. Feng, L. L. Hu, Y. H. Zhang, Q. N. Nie, H. J. Pei, C. Yang, J. K. Deng, C. G. Bao, J. X. Song, *Adv. Energy Mater.* **2022**, *12*, 2200568.
[3] J. Liu, Z. Bao, Y. Cui, E. J. Dufek, J. B. Goodenough, P. Khalifah, Q. Li, B. Y. Liaw, P. Liu, A. Manthiram, Y. Shirley Meng, V. R. Subramanian, M. F. Toney, V. V. Viswanathan, M. Stanley Whittingham, J. Xiao, W. Xu, J. Yang, X.-Q. Yang, J.-G. Zhang, *Nat. Energy* **2019**, *4*, 180.
[4] B. D. Adams, J. Zheng, X. Ren, W. Xu, J.-G. Zhang, *Adv. Energy Mater.* **2018**, *8*, 1702097.
[5] A. C. Kozen, C.-F. Lin, A. J. Pearse, M. A. Schroeder, X. Han, L. Hu, S.-B. Lee, G. W. Rubloff, M. Noked, *ACS Nano* **2015**, *9*, 5884.
[6] J. Xiao, Q. Li, Y. Bi, M. Cai, B. Dunn, T. Glossmann, J. Liu, T. Osaka, R. Sugiura, B. Wu, J. Yang, J.-G. Zhang, M. Stanley Whittingham, *Nat. Energy* **2020**, *5*, 561.
[7] K. J. Harry, D. T. Hallinan, D. Y. Parkinson, A. A. MacDowell, N. P. Balsara, *Nat. Mater.* **2014**, *13*, 69.
[8] H. Kühnle, E. Knobbe, E. Figgemeier, *J. Electrochem. Soc.* **2022**, *169*, 40528.
[9] H. Liu, W. Jiang, W. Chen, Q. Lin, S. Ren, Y. Su, R. Tong, Y. Zhang, *J. Mater. Chem. A* **2024**, *12*, 3575.
[10] M. Romio, J. Kahr, E. Miele, M. Krammer, Y. Surace, B. Boz, P. Molaiyan, T. Dimopoulos, M. Armand, A. Paolella, *Adv. Mater. Technol.* **2024**, *9*, 2301902.
[11] H. Kühnle, E. Knobbe, E. Figgemeier, *J. Electrochem. Soc.* **2021**, *168*, 20510.
[12] R. I. Hartley, *Int. J. Comput. Vision* **1999**, *35*, 115.
[13] S. L. Bangare, A. Dubal, P. S. Bangare, S. T. Patil, *Int. J. Appl. Eng. Res.* **2015**, *10*, 21777.
[14] N. Otsu, *IEEE Trans. Syst., Man, Cybern.* **1979**, *9*, 62.
[15] J. Serra, *Signal Process.* **1994**, *38*, 3.
[16] A. K. Cherri, A. A. S. Awwal, M. A. Karim, *Opt. Commun.* **1991**, *82*, 441.
[17] N. Kanopoulos, N. Vasanthavada, R. L. Baker, *IEEE J. Solid-State Circuits* **1988**, *23*, 358.
[18] I. Sobel, G. Feldman, *A talk at the Stanford Artificial Project in* **1968**, *1968*, 271.
[19] A. Bahrammirzaee, *Neural Comput. Appl.* **2010**, *19*, 1165.
[20] S. W. Smith, B. Walsh, K. Grauer, K. Wang, J. Rapin, J. Li, W. Fennell, P. Taboulet, *J. Electrocardiol.* **2019**, *52*, 88.
[21] Y. Zhang, H. G. Soon, D. Ye, J. Y. H. Fuh, K. Zhu, *IEEE Trans. Ind. Inf.* **2020**, *16*, 5769.
[22] I. Woo, A. Lee, S. C. Jung, H. Lee, N. Kim, S. J. Cho, D. Kim, J. Lee, L. Sunwoo, D.-W. Kang, *Korean J. Radiol.* **2019**, *20*, 1275.
[23] H. Alaskar, A. Hussain, N. Al-Aseem, P. Liatsis, D. Al-Jumeily, *Sensors* **2019**, *19*, 1265.
[24] D. Li, A. Cong, S. Guo, *Autom. Constr. 101*, 199.
[25] M. Ranzato, F. J. Huang, Y. -L. Boureau, Y. LeCun, *2007 IEEE Conf. on Computer Vision and Pattern Recognition*, Minneapolis, MN **2007**, pp. 1–8.
[26] A. Garcia-Garcia, S. Orts-Escolano, S. Oprea, V. Villena-Martinez, J. Garcia-Rodriguez **2017**, https://doi.org/10.48550/arXiv.1704.06857.
[27] W. Rawat, Z. Wang, *Neural Comput.* **2017**, *29*, 2352.
[28] L. Parisi, D. Neagu, R. Ma, F. Campean, *Expert Syst. Appl.* **2022**, *187*, 115892.
[29] S. R. Dubey, S. K. Singh, B. B. Chaudhuri, *Neurocomputing* **2022**, *503*, 92.
[30] H. Robbins, S. Monro, *Ann. Math. Statist.* **1951**, *22*, 400.
[31] L. Bottou, *Lecture Notes in Computer Science* (Eds: G. Montavon, G. B. Orr, K.-R. Müller), Springer Berlin Heidelberg, Berlin, Heidelberg **2012**, pp. 421–436.
[32] A. F. Frangi, W. J. Niessen, K. L. Vincken, M. A. Viergever, *Lecture Notes in Computer Science* (Eds: W. M. Wells, A. Colchester, S. Delp), Springer Berlin Heidelberg, Berlin, Heidelberg **1998**, pp. 130–137.
[33] M. Sokolova, G. Lapalme, *Inf. Process. Manage.* **2009**, *45*, 427.
[34] Intelligent Computing and Networking, in *Lecture Notes in Networks and Systems* (Eds: V. E. Balas, V. B. Semwal, A. Khandare), Springer Nature Singapore **2003**, https://doi.org/10.1007/978-981-99-0071-8.

[35] R. Dror, L. Peled-Cohen, S. Shlomov, R. Reichart, in *Synthesis Lectures on Human Language Technologies*. Springer International Publishing AG, Cham, Switzerland **2020**, p. 25.
[36] H. Makimoto, M. Höckmann, T. Lin, D. Glöckner, S. Gerguri, L. Clasen, J. Schmidt, A. Assadi-Schmidt, A. Bejinariu, P. Müller, S. Angendohr, M. Babady, C. Brinkmeyer, A. Makimoto, M. Kelm, *Sci. Rep.* **2020**, *10*, 8445.
[37] E. Sagheb, T. Ramazanian, A. P. Tafti, S. Fu, W. K. Kremers, D. J. Berry, D. G. Lewallen, S. Sohn, H. Maradit Kremers, *J. Arthroplasty* **2021**, *36*, 922.
[38] H. Christiansen, M.-L. Chavanon, O. Hirsch, M. H. Schmidt, C. Meyer, A. Müller, H.-J. Rumpf, I. Grigorev, A. Hoffmann, *Sci. Rep.* **2020**, *10*, 18871.
[39] N. Rospars, M. Srout, C. Fu, G. Mourouga, M. Mensi, A. Ingenito, *Commun Mater.* **2024**, *5*, 179.
[40] M. Golozar, P. Hovington, A. Paolella, S. Bessette, M. Lagacé, P. Bouchard, H. Demers, R. Gauvin, K. Zaghib, *Nano Lett.* **2018**, *18*, 7583.
[41] R. Schmitz, R. Müller, S. Krüger, R. W. Schmitz, S. Nowak, S. Passerini, M. Winter, C. Schreiner, *J. Power Sources* **2012**, *217*, 98.
[42] G. M. Hobold, J. Lopez, R. Guo, N. Minafra, A. Banerjee, Y. Shirley Meng, Y. Shao-Horn, B. M. Gallant, *Nat. Energy* **2021**, *6*, 951.
[43] X.-R. Chen, C. Yan, J.-F. Ding, H.-J. Peng, Q. Zhang, *J. Energy Chem.* **2021**, *62*, 289.
[44] M. Abdollahifar, A. Paolella, *Batteries & Supercaps* **2025**, *8*, e202400505.
[45] R. Zhang, X. Shen, Y.-T. Zhang, X.-L. Zhong, H.-T. Ju, T.-X. Huang, X. Chen, J.-D. Zhang, J.-Q. Huang, *J. Energy Chem.* **2022**, *71*, 29.